1 **Biosorption of Pb(II) Ions through Nanostructured Teff Straw based Magnetized Activated**

2 **Biocarbon: Aspects on Modeling, Optimization, and Kinetics**

3 Mohanasundaram Sugumar[1], Selvaraj Bharathi [2], Venkatesan Sampath[3], Venkatesa

4 Prabhu Sundramurthy [4,5,]*, Mayakannan Selvaraju[6], Shine Kadaikunnan[7], and Jamal

5 Mohammed Khaled[7]

6 [1]Department of Biochemistry and Crop Physiology, SRM College of Agricultural

7 Sciences, SRM Institute of Science and Technology, Baburayanpettai – 603201,

8 Maduranthagam Taluk, Chengalpattu District, Tamil Nadu, India.

9 [2]Department of Research Analytics, Saveetha Dental College and Hospitals, Saveetha

10 Institute of Medical and Technical Sciences, Saveetha University, Chennai – 600 007, India

11 [3]Department of Biochemistry, Sri Sankara Arts and Science College (Autonomous),

12 Enathur, Kanchipuram - 631561, Tamilnadu, India

13 [4]Centre for Natural Products and Functional Foods, Karpagam Academy of Higher

14 Education, Coimbatore, 641 021, Tamil Nadu, India.

15 [5]Department of Biotechnology, Faculty of Engineering, Karpagam Academy of Higher

16 Education, Coimbatore -641 021, Tamilnadu, India.

17 [6]Department of Mechanical Engineering, Rathinam Technical Campus, Coimbatore –

18 641021, Tamil Nadu, India.

19 [7]Department of Botany and Microbiology, College of Science, King Saud University, P.

20 O. Box 2455, Riyadh 11451, Saudi Arabia.

21 ***Corresponding Author:** Venkatesa Prabhu Sundramurthy (E-mail: haiitsvp@gmail.com)

22

23

24 **Abbreviations**:

25 % - Percentage

26 ˚C – Degree Celsius

27 AAS - Atomic absorption spectrometry

28 ABC - activated carbon

29 CCD- Central composite design

30 FTIR - Fourier transform infrared spectroscopy

31 ml – Milliliter

32 NTSAC- Nano-structured teff straw based activated carbon

33 Pb(II) – Lead(II) ions

34 pH – Potential of hydrogen

35 SEM - Scanning electron microscopy
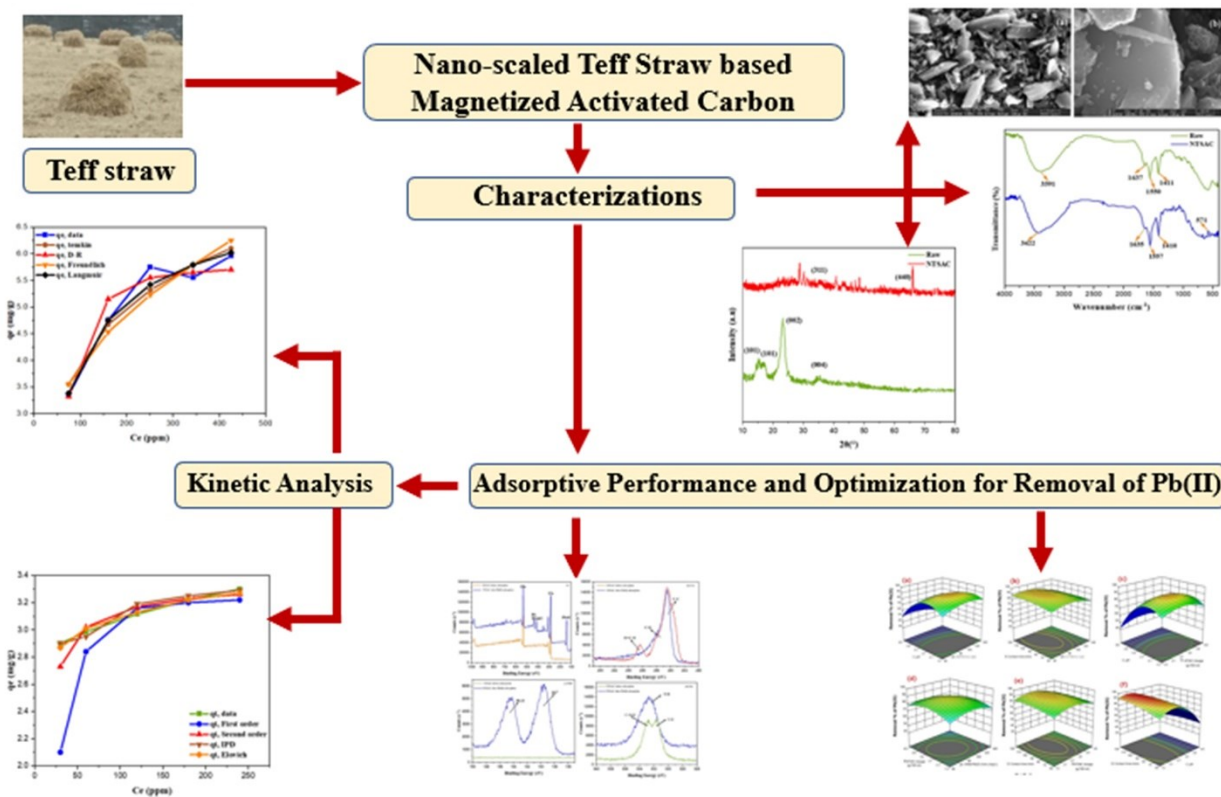
36 TS- Teff straw

37 XRD - X-ray diffraction

38

39

40

41   **GRAPHICAL ABSTRACT**

42

43   **Abstract**

44   In this study, activated carbon (AC) was prepared from teff grass straw via chemical activation

45   and microwave-assisted pyrolysis. The AC was modified by magnetization followed by it was

46   characterized by particle size, FTIR, XRD, thermogravimetric study, pore size, and magnetic

47   properties. Further, it was evaluated for its adsorptive removal performance of lead (II) ions from

48   aqueous solution. A statistical model was developed by response surface method (RSM) and the

49   crucial parameters, concentration of initial Pb(II), biosorbent loading, solution pH, and contact

50   time were optimized for maximizing the adsorption of Pb(II) ions. The optimal values were 95.36

51   mg/L, 0.656 g/100 mL, 5.5, and 88.7 min, respectively for aforementioned parameters. Under the

52   optimal condition, the Langmuir isotherm exhibited the most accurate correspondence with the

53   obtained experimental data. The findings from the kinetic analysis were found to be statistically

54   fit to the pseudo-2nd order model.

57

58   1   Introduction

59   The need of clean water is under increasing threat due to pollution caused by industrial, residential,

60   and agricultural practice (Rahman et al., 2021). Wastewaters that properly untreated before being

61   released into the environment should be concerned seriously because it causes inadequate hygiene

62   services which is highly endangers to natural ecology due to different contaminants (Naidu et al.,

63   2021). Among these contaminants, heavy metal ions are considered as extremely hazardous since

64   they combine with other environmental components like soil, water, or air and can expose to

65   humans and other living things through the food chain (Qasem et al., 2021). They mainly come

66   from the manufacturing process, particularly, paint factories, tanneries, battery plants, and other

67   refineries. In this regard, lead [Pb(II)] is one of the most dangerous heavy metal pollutants because

68   it can cause a wide range of health problems in humans, including dizziness, headaches, nausea,

69   and stomach problems (Balasubramanian et al., 2020). Unlike other metals like zinc, copper, and

70   manganese, which have biological purposes, lead is a poisonous heavy metal that seriously

71   interrupts several biological functions in plants and animals (Levin et al., 2021). Lead's damaging

72   effects have been subjected of numerous researches, and one of these used the Microtox Assay to

73   compare and contrast the relative toxicity of other metals (Kumar et al., 2022). According to the

74 World Health Organization, 0.01 mg/L is the absolute maximum level of Pb that should be present

75 in drinking water. Hence, necessary precautions to safeguard the people from Pb(II) exposure is

76 extremely crucial in order to prevent harmful impacts (Raj & Das, 2023). Keeping view in this

77 concern, many kinds of wastewater treatment have been developed to get rid of Pb(II) and its the

78 harmful effects, such as chemical precipitation, adsorption, filtration, ion exchange membrane

79 separation, coagulation, and osmosis.

80 However, heavy metals, like Pb are difficult and expensive to remove on a large scale, and current

81 methods are inefficient, complicated, and not very selective. In contrast, adsorption technique

82 using biosorbents is low expensive method and its effectiveness has made it a well-recognized

83 approach for the removal of many heavy metals (Dąbrowski, 2001). However, the selection of a

84 suitable biosorbent play a crucial role with respect to adsorption efficiency, pollutant selectivity,

85 reusability, and adsorption capacity for the intended use (Sharmiladevi et al., 2024). Accordingly,

86 several heavy metals have all been researched using different range of biosorbents. Historically,

87 the biosorbents derived from sugarcane bagasse, peanut shells, *Arundinaria alpina*, coffee husk,

88 etc. have been well-proven to produce excellent results in removing heavy metals (Chen et al.,

89 2020). Notwithstanding, preparation of green-based biosorbent material from agricultural residues

90 gains significant attention that can be addressed by valorizing the agro-wastes. The possibility of

91 using different bio-based adsorbents made from agricultural sources for the uptake of the

92 hazardous metal elements have been documented elsewhere. According to previous studies, the

93 adsorption capacity varies widely dependent on the nature of the bio-based absorbents and the

94 type of heavy metal being absorbed (Ighalo & Adeniyi, 2020).

95   In this line, the capacity of various materials for adsorbing Pb(II) from contaminated water has

96   been investigated through the use of different biosorbent materials (Awad et al., 2020). In this

97   light, activated carbon (AC) is one of the promising biosorbents that can be derived from

98   lignocellulosic materials. According to Surafel et al., the AC derived from teff hay biomass has

99   shown an excellent result for adsorptive removal of Pb(II) ions from aqueous solution (Beyan et

100   al., 2024). At the optimum treatment condition, the authors observed a 99.8% Pb(II) removal by

101   AC obtained from teff hay. In another study, the performance of titanate nanoflowers for

102   adsorptive removal of Pb(II) and its process kinetics were examined by Huang et al. (Huang et al.,

103   2012). According to them, titanate nanoflowers exhibited promising results for Pb(II) removal and

104   it was observed that the pseudo-2nd order kinetics and the Langmuir isotherm have provided an

105   exceptional fit to the experimental data. Hu and Shipley carried out an adsorption study using TiO_2

106   nanoparticles. They found that the adsorption efficacy around 95% after a fourfold regeneration

107   cycle at an optimal pH of 2 (Hu & Shipley, 2012).

108   Similarly, biosorbents were prepared from avocado seeds and used to effectively remove

109   chromium and lead from aqueous solution (Aiyesanmi et al., 2022). Both the natural and

110   chemically activated adsorbents had shown removal efficiencies of over 80% of heavy metal at

111   the operating temperature 45 °C and solution pH 5 (Leite et al., 2018). In study elsewhere, Ameen

112   et al. prepared biochar from the agricultural wastes of palm to examine the adsorption competence

113   of copper and lead (Ameen et al., 2022). They reported that the adsorption of 99 mg/g was

114   determined to be the maximized adsorption capacity for Pb(II) by the developed biochar material.

115   By altering several operating settings, Bagali et al. investigated the kinetics of the adsorption of

116   Pb(II) ions while using a banana's pseudo-stem derived AC (Bagali et al., 2017). Recently,

117   researchers have synthesized an inexpensive and environmentally friendly solid-phase AC made

from coffee husk waste. It allowed for a maximum removal of 98% Pb(II) with an adsorption capacity of 19 mg/g (Gonçalves et al., 2013a). Though several authors have mentioned different types of agricultural waste in their AC formulations for removal of lead, utilization of teff straw has not been studied extensively and still it is underutilized for biosorbents preparation (Kifetew et al., 2023). The agricultural residue, teff straw (TS) is a common and naturally occurring lignocellulosic waste in Ethiopia (Sundramurthy et al., 2024).

The teff plant accounted for about 25% of Ethiopia's total harvest, making it the country's most important agricultural residue. The teff plant is considered agricultural trash once the seed has been harvested. Bio-based AC/adsorbent can be less expensive to produce than the adsorbent made from more expensive precursors, given that lignocellulosic material, TS, has no economic usefulness and is merely undesirable solid waste (Tessema et al., 2023). So, the originality of this study is in its use of preparing activated carbon from TS to propose remediation measures for Pb(II) removal from wastewater.

In this study, a chemical activation method was adopted to prepare AC using TS, which was then subjected to magnetization. Because of their exceptional adsorption capacity and strong magnetism property, magnetic adsorbents gain more attention in treating environmental contamination. Furthermore, the prepared adsorbent was evaluated for adsorption removal capability of Pb(II) ions by batch mode. Response surface method (RSM) in conjunction with the central composite design (CCD) was utilized to improve the absorption efficiency. Additionally, the kinetics, isotherm model, and thermodynamic investigations were evaluated using the adsorption data. Furthermore, desorption and regeneration studies were also performed to explore more about the adsorptive-potential of prepared adsorbent for its reuse.

2 Experimental methodology

2.1 Materials

TS was obtained on farmland in Addis Ababa, Ethiopia, after the teff seeds had been harvested during the month of March 2022. TS sample has been transported to SRM Institute of Science and Technology, India using airtight containers to carry out the experiments. The TS was washed multiple times with tap water and then with deionized water to eliminate dust and other contaminants before being dried in an oven set to 65 ℃ for two days. To acquire the necessary particle size for this investigation, it was first pulverized and then sieved. For experimentation, distilled water, zinc chloride ($ZnCl_2$), potassium nitrate (KNO_3), sodium chloride (NaCl), and lead nitrate [$Pb(NO_3)_2$] were utilized. Hydrochloric acid and Sodium hydroxide were employed to achieve the desired pH level. An atomic absorption spectrophotometer (AAS) (PerkinElmer, Model-PINAACLE 900T) was utilized in accordance with standard protocols to ascertain the quantity of Pb(II) ions.

2.2 AC preparation, Magnetization, and Nano-biocarbon Preparation

Initially, the TS powder was subjected to impregnation with $ZnCl_2$ (1:1 ratio), then, the activated carbon was produced by microwave pyrolysis technique (Oliveira et al., 2009). After impregnation, a homogenous paste was made by blending the with 0.05L of sterile water. The paste that formed was placed in a quartz container for pyrolysis with 2.5 mL/sec of inert N_2 gas. Microwave pyrolysis facilitates more extensive pyrolysis decomposition compared to the conventional pyrolysis. It is a thermochemical technique, which makes use of electromagnetic waves with the dipoles that interact with the heated material. As a result, heat is created inside the target material rather than coming from an outside source, which makes the heating process easier

8

162   to manage and more efficient in terms of uniform heat distribution. After the pyrolysis, a flow of

163   inert N_2 at 2.5 ml/sec was used to cool the sample. Then, the resulted material was immersed in a

164   solution of distilled water and hydrochloric acid (1:1) at 85 $^{\circ}$C for 120 min. The sample matrix had

165   inorganic chemicals leached out throughout this process (Zhao et al., 2022). Excessive washing

166   with distilled water was applied to resultant carbonaceous materials until the washing water's pH

167   reached to 7. Next, it was subjected to a drying process in an oven set at 85 $^{\circ}$C with a constant

168   airflow for a duration of 12 h.

169   Magnetization of AC has been prepared using a solution containing 2:1 molar ratio of

170   Fe^{3+}/Fe^{2+}. For this purpose, a solution containing 5.03 g $FeCl_3.6H_2O$ and 5.2 g $FeSO_4.7H_2O$ in 100

171   mL of distilled water (Varadharajan et al., 2022). The mixture was well stirred by for 15 min.

172   Then, prepared AC (5 g) was supplemented followed by the mixture was stirred for 20 min. During

173   this time, the solution was maintained at 60 $^{\circ}$C. Moreover, the slurry mixture was lowered in

174   temperature to 35 °C. Then, the necessary amount of sodium hydroxide (5 mol/L) was added to

175   the solution to bring the solution pH level down to 10. A magnetic field was applied to separate

176   the magnetized AC that had been mixed continuously for 8 h. Further, it was cleaned with ethanol.

177   A vacuum drier was used to dry the obtained magnetized AC sample, and then it was sealed in an

178   airtight container. It was kept in a cool, dry environment. Additionally, in order to achieve

179   nanostructured material, the particle size was reduced using ball milling technique. Ball milling is

180   one of the oldest and most reliable ways to make nanostructured materials. In this study, planetary

181   centrifugal ball mill was used. For grinding purpose, stainless steel balls (no of balls, 800; radius,

182   1.3 mm; total weightage of the balls, 50 g) were utilized in this experiment. To prevent the balls

183   and biocarbon from overheating, 5-minute on/off timing of the ball milling experiment was carried

184   out. Using laser beam scattering equipment, the mean and distribution of particle size the

185 biocarbon sample was assessed after 14 h of milling. Particle size distribution was determined by

186 combining 1 mg of activated biocarbon with 0.5% Tween 80 and 1% ethanol in 200 mg of distilled

187 water for 50 min with the use of a magnetic stirrer.

2.3 Characterization of Nano-structured Teff Straw based Activated Carbon (NTSAC)

189 The physical-chemical properties of the NTSAC sample were analyzed for its characteristics by

190 following the procedures set out by the ASTM standard. To measure the point of zero charge (pzc),

191 the method reported by Kifetew et al. (Merine et al., 2024) was followed.

192 Further, surface morphology and elemental composition were examined using field emission

193 scanning electron microscopy (FESEM, QUANTA-250 FEG) and EDX (Bruker Xflash 6130)

194 techniques, respectively. The crystalline nature of the synthesized sample was analyzed with the

195 help of X-ray powder diffraction (XRD, Rigaku ULTIMA-IV). A Scherrer's equation [Equation

196 (1)] was used with XRD data to determine crystallinity (Igalavithana et al., 2017). Fourier

197 transform infrared spectroscopy (Bruker Tensor 27) at 400-4,000 cm^{-1} was used to determine the

198 available functional groups of NTSAC. The utilization of the BET (Brunauer-Emmett-Teller)

199 technique, which measures the nitrogen adsorption capacity of NTSAC at 77 K, the surface area,

200 pore size distribution, and pore volume were found using a BET instrument (Microtrac BELSORP-

201 mini II).

202
$$\text{Crystallinity} = \frac{\text{Crystalline peaks area}}{\text{All peaks area (amorphous + crystalline)}} \times 100 \qquad (1)$$

2.4 RSM-based statistical analysis on lead (II) adsorption

The effectiveness of adsorption process depends on several independent variables, such as adsorbent type and amount, the process temperature, the stirring speed, particle size of the adsorbent, the processing time, and the solution pH (Tee et al., 2022). In research elsewhere, with aiming to enhance the adsorptive removal of Pb(II) ion by the selective adsorbent, optimal circumstances have been identified by multiple researchers. In the present study, the influence of independent factors, the initial concentration of Pb(II) ions, adsorption period, solution pH, and dosage of NTSAC were considered to investigate by a batch-based adsorption study. For adsorption experiments, a conical beaker (0.1 L volume of each sample) with a thermostatic stirrer set to room temperature was operated with 200 rpm shaking speed. Clear liquid was obtained by filtering the mixture through Whatman No. 1 filter paper, and then the amount of Pb(II) ion residue was determined using atomic absorption spectrometry (AAS) at 217 nm. A blank solution was also analyzed alongside each sample. Equation 2 was employed to compute the percent removal of Pb(II) adsorption by NTSAC subsequent to the determination of the adsorption capacity (Equation 2) (Jagadeesh & Sundaram, 2023).

$$\text{Efficacy Removal}(\%) = \frac{C_o - C_f}{C_o} \times 100 \qquad (2)$$

$$Q\left(\frac{mg}{g}\right) = \frac{C_o - C_f}{m} \times V \qquad (3)$$

Where, C_o is initial Pb(II) concentration in mg/l, C_f is final Pb(II) concentration in mg/l, m is adsorbent mass in g, V is volume of the solution in ml.

222 In the present study, the optimum value for the chosen independent parameters, namely, NTSAC

223 dose, adsorption time, pH, and initial concentration of Pb(II) were statistically analyzed for

224 maximizing Pb(II) removal from the synthetic solution. During experimentation, the agitation

225 speed was maintained at a constant rate of 200 rpm, while the temperature was held at room

226 temperature. Response surface methodology (RSM) is a statistic technique which is used for

227 interaction investigation and to optimize process parameters. When designing experiments, RSM

228 approach is frequently employed to reduce the number of trials for a given number of parameters

229 and their values. Herein, the RSM analysis was carried out using selected variables that were

230 chosen to optimize by grouping via central composite design (CCD) approach. It guarantees a

231 comprehensive analysis of all pertinent components and their interrelationships. With their

232 corresponding levels, the chosen variables are listed in Table 1. CCD suggested a series of 30 trials

233 according to the limitations figure, validate axial, factorial, and average levels. Consequently, the

234 average adsorption was considered value by looking at each experiment three times. Using RSM

235 analysis a polynomial equation model (Equation 4) was constructed that describes the relation

236 between the experimental response and the chosen parameters.

237
$$R = \theta_0 + \sum_{j=1}^{4} \theta_j Y_j + \sum_{j=1}^{4} \theta_{jj} Y_j^2 + \sum_{i}^{4} \sum_{<j=2} \theta_{ji} Y_i Y_j + e_i \qquad (4)$$

238 Where, R is response [(%) removal of Pb(II)], θ_0 refers the intercept coefficient, e_i is known as

239 correlation error.

240 In addition, statistical optimization was used on the process variables with the aim of maximizing

241 the Pb(II) removal. All statistical restraints were evaluated with ANOVA (analysis of variance).

242 The optimum values were determined by solving the regression equation containing the selected

243 variables. Using a response surface map, the interaction among the factors were analyzed. In this

244 regard, Design-Expert 12 was used to developed RSM and CCD probes. The created model was

245 confirmed through a triple experimental run, as expected by the design expert (Duan et al., 2023).

246 Table 1 Input factors and its levels for biosorption study.

Factors	Factor coding	Unit	-α	-1	-1	+α
Initial Pb (II) concentration	A	mg/L	20	60	140	180
NTSAC dosage	B	g/100 ml	1	2	4	5
Contact time	C	min	30	60	90	150
Solution pH	D	–	1.5	2	3	3.5

247

248 **2.5 Equilibrium Adsorption Studies**

249 The experimental findings were correlated and the adsorption mechanisms were evaluated using

250 the adsorption isotherm models, namely, Freundlich, Temkin, Dubinin - Radushkevich (D-R) and

251 Langmuir (Rose et al., 2023). Langmuir isotherm model evaluates the monolayer adsorption on a

252 uniform adsorbent surface, where the adsorption sites are all the same and have the same

253 adsorption energy. The equations, (3) and (4), reflect the linear and nonlinear Langmuir models,

254 correspondingly (Mohammadpour et al., 2023).

$$\frac{C_e}{q_e} = \frac{1}{q_m k_L} + \frac{C_e}{q_m} \qquad (3)$$

$$q_e = \frac{q_m k_L C_e}{1 + k_L C_e} \qquad (4)$$

255 Here, q_e (mg/g) is amount of Pb ions adsorbed by an equilibrium mass of adsorbent, q_m (mg/g)

256 denotes the Pb ion monolayer formation capacity at maximal adsorption capacity as a function of

257 adsorbent mass, C_e (mg/L) is the equilibrium Pb ions in in the aqueous solution. k_L (L/mg) refers

258 the adsorption energy which is a constant for the Langmuir isotherm.

259 The Freundlich model relies on the fact that adsorbent surfaces are typically not perfectly smooth,

260 and that different adsorption sites have variable enthalpies of adsorption. Equations (5) and (6) can

261 be used to depict the Freundlich isotherm (Karuppaiyan et al., 2023).

$$\ln q_e = \frac{1}{n}\ln C_e + \ln k_f \qquad (5)$$

$$q_e = k_f C_e^{1/n} \qquad (6)$$

262 Herein, k_f denotes the adsorption capacity; n refers the non-linearity of the function. The factors,

263 n and k_f, can be computed using the plot developed from the $\ln(q_e)$ versus $\ln(C_e)$.

264 When assessing the possibility for adsorbate/adsorbent interactions, the Temkin (T) isotherm can

265 be used to measure the interface between ion concentrations. The Temkin isotherm model can be

266 represented by the equations (7) and (8) (Karuppaiyan et al., 2023).

267

$$q_e = \frac{RT}{b}\ln(AC_e) \qquad (7)$$

$$q_e = \frac{RT}{b}[(\ln k_T + l\, n(C_e)] \qquad (8)$$

268 Herein, b and K_T (L/mol) are the Temkin constants, b is adsorption of heat constant (J/mol), T

269 refers absolute temperature constants (K), R is gas constant (8.314 J/mol K).

270 The D-R model performs exceptionally well in the concentration range of medium to high

271 concentrations because of this model well-correlates the multilayer adsorption property due to

272 physical adsorption. The equations, (9) and (10) represent the D-R model (Zhang et al., 2024).

$$\ln q_e = \ln q_m - k_D \varepsilon^2 \qquad (9)$$

$$\text{Where, } \varepsilon = RT \ln \left(1 + \frac{1}{C_e}\right) \qquad (10)$$

273 where, k_D (mol^2/kJ^2) is a constant proportional to the enthalpy of adsorption, ε Polanyi potential

274 that can be obtained from equation (10), E (kJ/mol) is free energy (kJ/mol). This represents the

275 adsorption energy that can be determined by the equation (11) using the value of k_D.

$$E = \frac{1}{\sqrt{2K_D}} \qquad (11)$$

2.6 Kinetic Approaches on Adsorption

277 To conduct the kinetic analysis, 5 g of adsorbent was used. The experiment solution contained 0.1

278 L of 100 ppm Pb(II) ions supplemented with 5 g of NTSAC. The mixture was continuous agitated

279 at 250 rpm for required time. In the first half an hour, aliquots were taken at regular intervals of 5

280 min due to the rapid adsorption process preceding saturation. Then, for the next 5 hours, the

281 samples were taken at the 60-min mark. To assess their suitability for the kinetic data, various

282 models were evaluated, such as pseudo-1st order, pseudo-2nd order, Elovich kinetic, and

283 intraparticle diffusion. The pseudo-1st-order and 2nd order kinetic models are described by the

284 equations, (12) and (13), respectively (Cao et al., 2024).

$$\ln{(q_e - q_t)} = \ln{(q_e)} - k_1 t \tag{12}$$

285   where, q_t refers quantity of adsorbed Pb(II) at any time t (mg/g), q_e refers quantity of adsorbed

286   Pb(II) at the equilibrium stage. k_1 refers the pseudo-1st-order kinetic constant (Debnath & Das,

287   2023).

$$\frac{1}{q_t} = \frac{1}{k_2 q_e^2} + \frac{t}{q_e} \tag{13}$$

288   When the adsorption rate is controlled by the diffusion of adsorbate, the intra-particle diffusion

289   kinetic model (equation 14) outperforms the other models while fitting the kinetic data. The

290   significance of particle diffusion during adsorption can be explained by the linearity of the fitness

291   function which defined by the intraparticle diffusion model (Danish et al., 2022).

$$q_t = k_{dif} t^{1/2} + C \tag{14}$$

292   While plotting 'q_t' *vs* '$t^{1/2}$', the width of the boundary layer (C) can be determined from the

293   intercept value. This value is used to calculate the external mass transfer resistance.

294   Elovich kinetic is an additional prominent kinetic model that can be employed to analyze the

295   kinetics and adsorption mechanism. The Elovich kinetic model is stated in its streamlined form by

296   equation (15). According to this model of equation, the linear relationship between 'q_t' vs 'ln(t)'

297   has a slope of ($1/a_E$) and an intercept of ($1/a_E$) ln ($a_E b_E$) (Al-Hazmi et al., 2024).

$$q_t = \frac{1}{a_E} \ln(b_E a_E) + \frac{1}{a_E} \ln(t) \tag{15}$$

298   Where, a_E is constant of desorption (g/mg); b_E denotes rate of initial adsorption (mg/min).

299

300   **3. Results and Discussion**

301   **3.1 Characteristics of NTSAC**

3.1.1 Physiochemical characterization

The adsorption approach has certain limitations when it applies for removing heavy metals from aqueous solutions. Proximity analysis results for NTSAC and other agricultural biomasses are tabulated in Table 2. According to the NTSAC's physiochemical characterization, the percentage of fixed carbon was found to be high. These results were foreseen due to the presence of these elements in the cellulose, hemicellulose, and lignin molecules. In general, heavy metal removal by adsorption can be facilitated by materials rich in lignocellulosic content, which contain different functional groups including hydroxyl, amines, and carboxyl. The amount of water vapor present in a substance was characterized by its moisture content (MC). The MC, AC, and VM of obtained NTSAC sample, a porous material, were all found to be less. If the biocarbon sample has a high ash content, it will have a low adsorption capability. There were fewer non-carbon components while compared to the primary carbon analogue. NTSAC qualities with a higher FCC and CY content might be claimed as graphitization grade. NTSAC's high CY and FCC content made it as a promising adsorbent candidate. NTSAC's FCC and CY were also noticeably higher than those of other lignocellulose-based ACs, like those made from corncob and coffee husk (Gonçalves et al., 2013b; Song et al., 2013). Bulk density (BD) value for agricultural waste adsorbent that is intended for use as AC should not exceed 0.25 g/cm^3. According to the results, the NTSAC's bulk density of 0.76 g/cm^3 made it met the previously mentioned requirement. pH has significant impact on the adsorption of Pb(II) ions by NTSAC. In this line, the it has been found that adsorbent can be effective at removing Cr^{6+}, Ni^{2+}, and Pb^{2+} since the biocarbon at pH value between 5.5 and 7.5. In addition, the resultant biocarbon sample has P_{ZC} value of 4.86, which promising that the lower P_{ZC} value is preferable with increased cation adsorption.

Table 2. Results on proximate analysis for NTSAC sample.

| Biomass	HY (%)	FCC (%)	A (%)	C (Mc/cm)	MC (%)	CY (%)	BD (g/cm^3)	VM (%)	SA (m^2/g)	P$_{ZC}$	pH
NTSAC	4.62	69.74	5.03	0.61	5.78	65.18	0.76	18.42	494.2	4.86	7.15

325 Where, HY - hydrogen yield; FCC - fixed carbon content; C - conductivity; A - ash content CY-

326 carbon yield; VM - volatile matter; SA - surface area; MC - moisture content; P$_{ZC}$ - point zero

327 charge; BD - bulk density

328 **3.1.2 Surface morphology**

329 The SEM has been used for many years to learn about the surface's shape and the adsorbent's

330 structure. Figure 1 depicts the SEM surface morphology of NTSAC sample. The surface

331 morphology was observed to be uneven and harsh in its surface structure. These biochar pieces

332 were found to be covered in aggregated particles after being magnetized. Following the

333 magnetization process, the aggregates' coating took on a crystal flake-like form. The

334 morphological shifts observed in materials treated with various iron salts have been confirmed by

335 numerous researches. Figure 2 illustrates the particle size distribution for the resultant NTSAC

336 sample. Santhosh et al. found in magnetized biochar samples derived from sludge and woodchips

337 structures resembling flake-shaped objects composed of aggregated Fe_2O_3 nanoparticles ranging

338 in size from 50 to 100 nanometers (Santhosh et al., 2020). The authors, Guel-Nájar et al., who

339 investigated the morphology of magnetized biochar prepared from corn straw, shown to a similar

340 conclusion (Guel-Nájar et al., 2023). The flakes of nano-dispersed oxide phase that coat the

341 biochar's pores and cavities increase its surface area and adsorption capability. According to

18

342　Mohan et al., magnetized biochar made from oak wood and oak bark has shown increased the

343　material's specific surface area (Mohan et al., 2014). However, after the TS was acid impregnated

344　activation, a large number of pores were found in the NTSAC. High temperatures during

345　processing damaged the lignocellulosic material, and the chemical vapors that were evaporated

346　left the material with intact stomates. This porosity on the surface may have a crucial role in the

347　binding of Pb(II) ions.

348
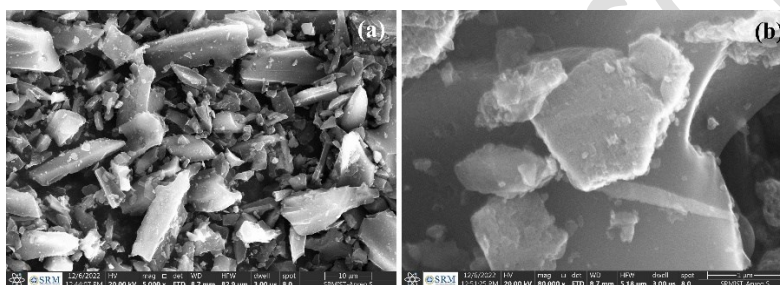
349

350　Figure.1 The SEM surface morphology of acquired NTSAC sample.
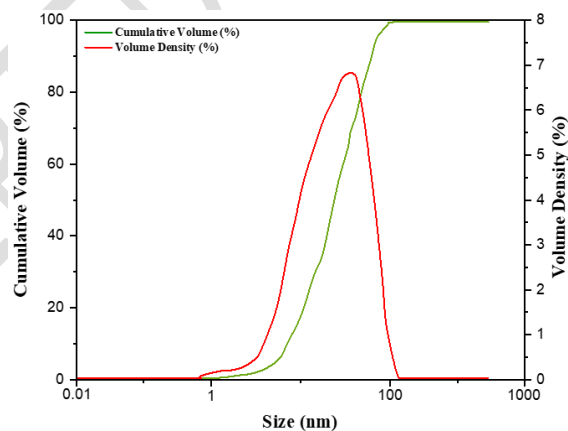
351

352　Figure. 2 Particle size distribution profile for resultant NTSAC sample.

353　**3.1.3 FTIR analysis for Functional groups**

354 The synthesized adsorbent materials' functional group content was examined by means of Fourier

355 transform infrared spectroscopy (FTIR). Figure 3 presents the FTIR spectra obtained from the

356 samples of raw TS powder and NTSAC. The FTIR examination results showed that the raw

357 material contained many different types of cellulose and organic functional groups. The stretching

358 vibration of the O-H bond was amplified at 3394 cm^{-1}. The fainter peaks at 2946 cm^{-1} and 2872

359 cm^{-1} indicated the C-H stretching vibration for alkanes. Hydroxyl bending, C-O stretching, and

360 aromatic C-C stretching were identified which attributed to the spectral peaks at 1639, 1552, and

361 1412 cm^{-1}, respectively (Dong et al., 2022). However, the FTIR spectra for magnetic biochar

362 showed changes after biocarbon magnetization, specifically between 400 and 600 cm^{-1}. The Fe-O

363 stretching mode in magnetite's octahedral and tetrahedral sites were indicated by a brief peak at

364 570 cm^{-1}. The absence of Fe(II) was indicated by the presence of weak absorption bands at 645cm

365 $^{-1}$, 604 cm $^{-1}$, and 449 cm $^{-1}$.

366 The results revealed that the sample had signatures unique to lignocellulosic-based biochar. The

367 FTIR spectrum of NTSAC was related to that of raw, and it was found that the intensity of various

368 bands had decreased. This was especially true for the bands at 3391 cm^{-1} and 1637 cm^{-1}, as well as

369 the bands at 1550 and 1411 cm^{-1}. The pyrolysis process has reduced the band intensities because

370 several functional groups in the raw material's components were destroyed by microwave

371 pyrolysis. For example, aliphatic hydroxyl groups in the biomass might subjected to thermal

372 degradation between 120 and 200 $^{\circ}$C. At temperatures above 400 $^{\circ}$C, aliphatic methylene, methyl,

373 and methoxy groups could be cleaved, and carboxyl and carbonyl groups were led to regenerate.

374 Therefore, the synthesis of biochar with significant carbonization was confirmed by the attenuation

375 of many peaks in the FTIR spectrum at 450 $^{\circ}$C.

376
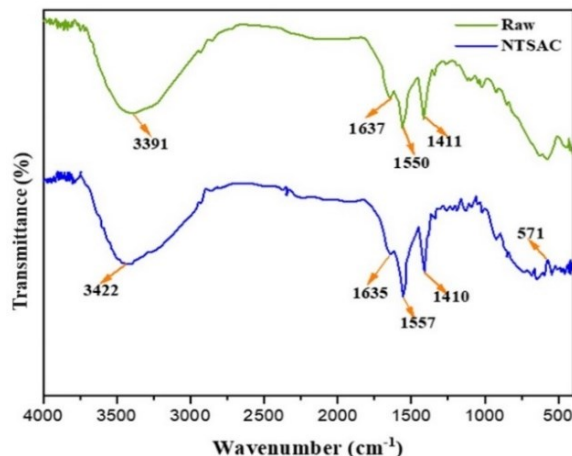
Figure. 3 Spectra obtained from FTIR analysis of raw material and prepared NTSAC.

3.1.4 XRD analysis

Figure 4 depicts the XRD spectra of both raw material and NTSAC. Diffraction peaks at 13.60, 17.60, 23.40, and 35.50 in the XRD pattern of raw sample was consistent with cellulose Iβ crystal lattices (101), (101), (200), and (004). The crystalline peaks associated with cellulose, according to Gan and Chow (Gan & Chow, 2021), may broaden and flatten when raw particle size decreases, especially below 150 μm. The XRD pattern seen by and NTSAC agreed well with the diffraction peak locations of 18.17, 31.12, 36.25, 42.9, 53.56, 57.41, and 62.98 as reported by Foroutan et al. (Foroutan et al., 2019). The XRD pattern of AC showed many, overlapping peaks. Biochar made at 450 ºC from a range of agricultural wastes showed XRD spectra that were very comparable to those of graphite, coquimbite, and hydrobiotite. New peaks at 36.25 and 66.98 were found after biocarbon magnetization, which correlate to magnetite's (311) and (440) lattices. The crystal-like flakes used as decoration for both the raw material and the NTSAC were found to be made primarily of an agglomeration of magnetite nano-crystals, as shown by the XRD profile of the magnetized adsorbents.

21

392
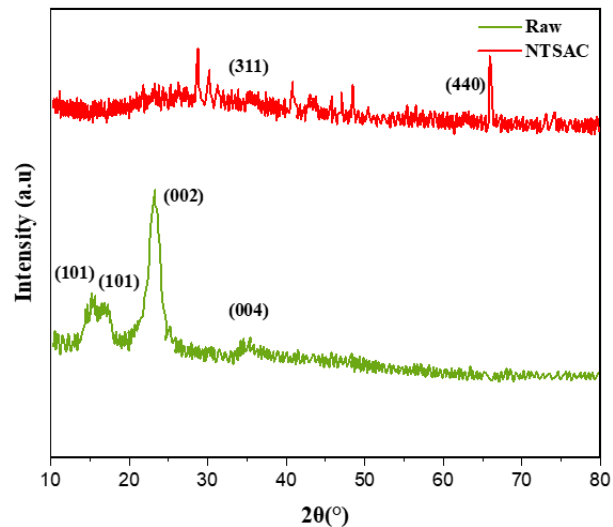
Figure. 4. XRD Spectra of raw material and resultant NTSAC sample.

393

The N_2 adsorption-desorption isotherms are illustrated in Figure 5. The presence of micropores

394

was indicated by the early section of the isotherms, which was of type I shape (IUPAC

395

classification) for the resultant carbon. In addition, the isotherm displayed a tiny capillary

396

condensation step at high P/P_o values and an H4-type hysteresis loop. According to the results, the

397

presence of both micro-porosity and a tiny part of meso-porosity can be concluded, and the

398

hysteresis loop, found for $P/P_o > 0.5$, can be attributable to capillary condensation in narrow slit-

399

shaped mesopores. Although the amount of N_2 adsorbed at high relative pressure was negligible,

400

this was because of the many mesopores present in the material. Variations in the amount of

401

nitrogen that remains after iron impregnation reflected shifts in textural characteristics. Since iron

402

incorporation may restrict the carbon pores, in this way limiting the surface area of the sorbent and

403

the number of accessible sites for adsorption. Sorbent made from modified carbon should have

404

their surface area quantified for this reason. Pre-magnetization S_{BET} values for AC were found to

405

be 973.65 m^2 g^{-1}, while results for the NTSAC sample showed a modest fall in S_{BET} values,

406

suggesting that iron metal impregnation can cause a drop-in surface area value. The same tendency

407

408 was observed for V_{tot} and V_{micro} levels. The deposition of iron oxide-based particles, which can fill

409 some of the vacuum spaces of the carbon materials, may be to blame for the reduction in surface

410 area and pore volume. However, the sorption capacity was improved which relates to the sorption

411 sites provided by these iron oxide-based particles.
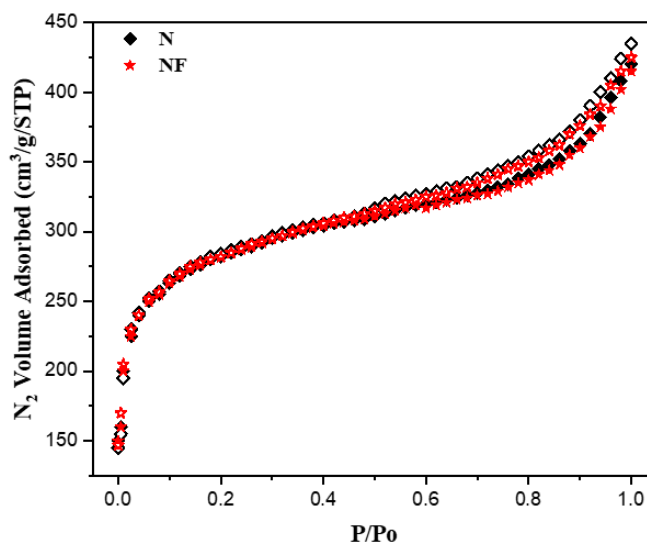

412

413 Figure. 5 Profiles of N_2 adsorption and desorption for the biocarbon sample before (N) and after

414 magnetization (NF)
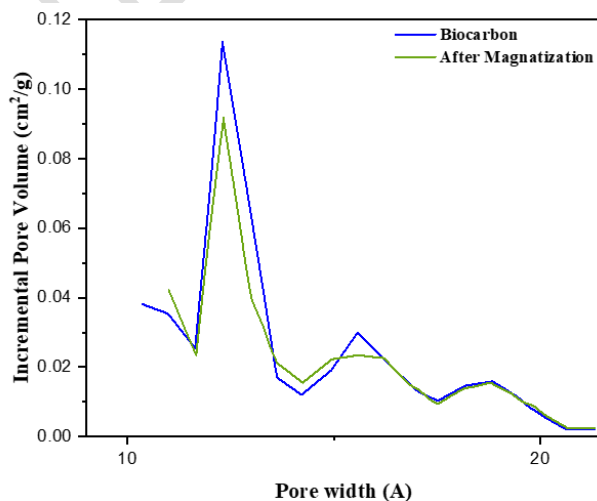
415

416 Figure. 6 Pore distribution for the biocarbon sample before and after magnetization

3.1.5 Thermal characteristics

418   Thermogravimetric analysis was used to deduce the time-dependent mass change of the adsorbent

419   in relation to the temperature change. The thermographic study of the resultant adsorbent is

420   depicted in Figure 6. According to the results, the weight loss in TS biocarbon was observed in

421   four stages: dehydration below 200 $^{\circ}$C, oxidation of aromatic compounds between 400 and 600

422    $^{\circ}$C, carbonate loss between 600 and 800 $^{\circ}$C, and residual ash breakdown around 800 $^{\circ}$C. In general,

423   the biocarbon made from various biomasses all go through these phases of weight reduction (Aziz

424   et al., 2023). Temperature changes, notably on the upper end, were noticed at the first and third

425   stages of weight reduction after magnetization. On the other hand, the second phase of weight loss

426   was accompanied with a peak-to-trough change. In magnetized biocarbon, the reduction and

427   volatilization of heavy metals cause a loss of mass between 800 and 900 $^{\circ}$C.
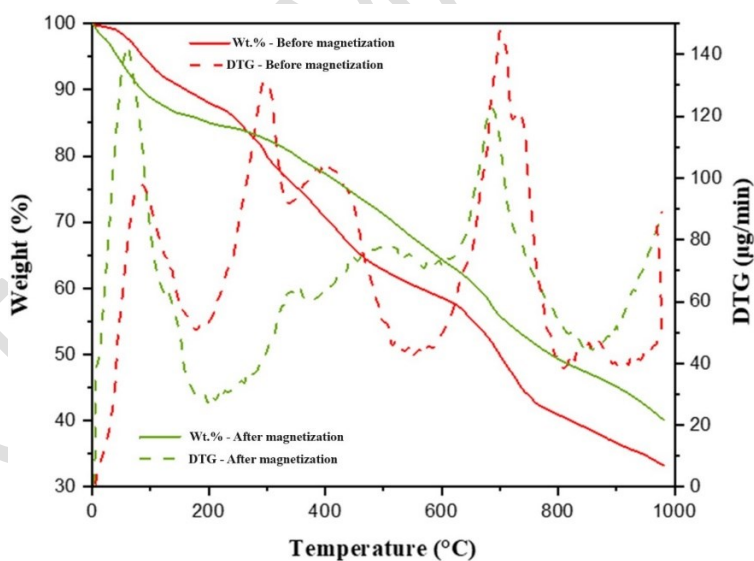

428

429   Figure. 6 TGA plots of before and after magnetization of biocarbon samples.

430

431   **3.1.6 Magnetic characteristics**

432   VSM analysis was used to examine the kind of magnetized NTSAC. The ferromagnetic character

433   of the synthesized bio-adsorbent was confirmed by Figure 7, which depicts its magnetic hysteresis

434   (M-H) curve. In terms of NTSAC, the values for M_s was determined to be 0.018 emu/g, M_r was

435   0.004 emu/g, and H_c was 106 O_e. The results were supported by Venkatramanan et al. who have

436   examined on magnetized cotton dust biochar (xx). Unwanted contaminants altered the magnitude

437   of the magnetic hysteresis loop in the same way as the crystal lattice's magnetic anisotropy does.

438   While compared to Wang and Zhang report, the hysteresis loop has been significantly reduced due

439   to the presence of non-magnetic crystals such as Fe_3O_4,. The adsorbents' high sensitivity to the

440   magnetic field was established despite their lower magnetic saturation (86-110 emu/g) compared

441   to that of bulk Fe_3O_4 (Wang & Zhang, 2020).

442
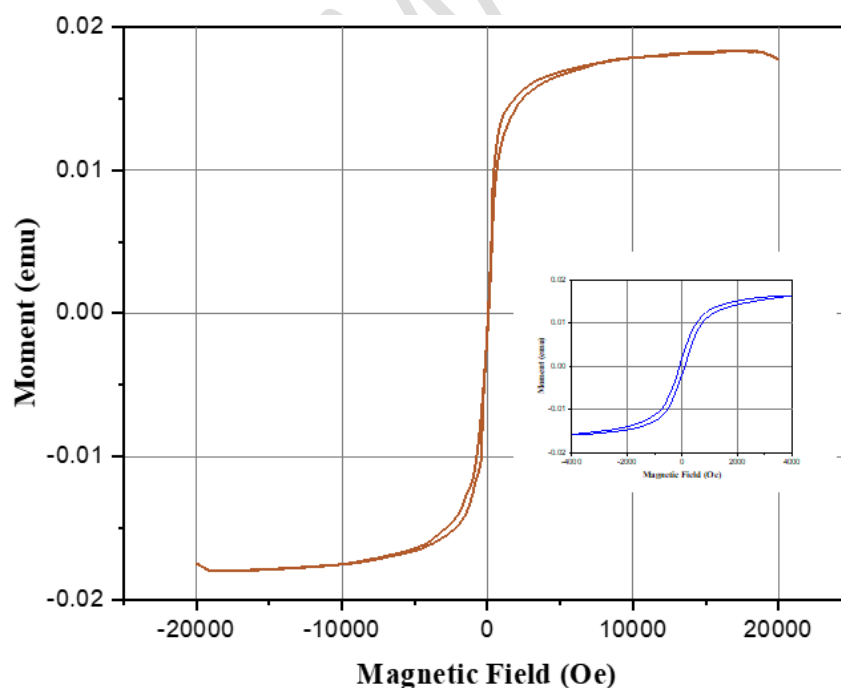
443

444   Figure. 7 VSM plots of NTSAC. The insert plot shows an expanded VSM plot with visible

445   hysteresis loop.

25

3.2 Adsorption of Pb(II) ions by NTSAC

3.2.1 Modeling and Optimization Analysis for Lead (II) ions Adsorption

Optimal removal capacities for batch-type adsorption have been calculated using a one-factor-at-a-time method. Based on earlier research, 5 levels were planned for each factor which are highly influencing the adsorption process. To improve the adsorption course parameters and select the best model for the process, the RSM-CCD method was applied. In 30 independently generated CCD experiments, the adsorption was examined as a function of initial Pb(II) concentration (A), dose of NTSAC (B), solution pH (C), and contact time (D). NTSAC exhibited a significant capacity for adsorptive removal of Pb(II) ion, ranging from 16.56 to 92.59 %, from a given solution (Table 3). Maximum discrepancy between the model's predicted value and the experiment's actual value was small, suggesting the two were in good agreement. Previous studies on the ability of various activated carbons derived from agricultural waste to remove Pb(II) ions have agreed with the present results (Al-Hazmi et al., 2024; Cao et al., 2024; Danish et al., 2022; Debnath & Das, 2023; Mohammadpour et al., 2023; Song et al., 2013; Zhang et al., 2024). The quadratic model was chosen for the RSM statistical modeling development because the predicted and adjusted R^2 values were 0.9524 and 0.9718, respectively, which were the highest that could be achieved. As a result, Table 4 indicates that, in terms of prediction success, the quadratic model was the best option for the existing configuration. Table 3. Independent characteristics of the CCD matrix in conjunction with the corresponding experimental and projected response.

Run	Factor 1	Factor 2	Factor 3	Factor 4	Response
	A: Initial Cr (VI) C (mg/L)	B: NTSAC dose g/100 ml	C: pH	D: Contact time (min)	Cr (VI) removal (%)

1	100	3	2.5	150	89.6
2	60	4	3	60	82.52
3	140	2	2	60	80.76
4	140	4	2	120	79.52
5	140	4	2	60	77.67
6	100	3	2.5	90	95.56
7	180	3	2.5	90	69.13
8	100	3	3.5	90	80.82
9	60	2	2	120	91.45
10	100	3	2.5	90	96.56
11	140	2	3	120	77.41
12	60	2	3	60	81.67
13	60	4	3	120	84.15
14	140	4	3	120	72.21
15	100	3	1.5	90	89.12
16	100	3	2.5	90	92.42
17	100	3	2.5	90	94.57
18	100	1	2.5	90	83.54
19	60	2	3	120	86.19
20	140	2	3	60	76.65
21	140	4	3	60	72.98
22	100	3	2.5	90	92.54
23	100	5	2.5	90	77.14

24	100	3	2.5	30	77.69
25	140	2	2	120	88.17
26	60	4	2	120	88.67
27	20	3	2.5	90	84.32
28	100	3	2.5	90	94.65
29	60	4	2	60	80.53
30	60	2	2	60	79.51

465

466   Table 4. Statistics of model summery

Source	Sequential p-value	Lack of Fit p-value	Adjusted R²	Predicted R²	
Quadratic	< 0.0001	0.9170	0.9718	0.9524	Suggested

467

468   Pb(II) removal (%) = - 92.608 + 0.8006 Initial Pb(II) Concentration + 23.984 NTSAC dose +

469   57.577 pH + 1.041 Contact time - 0.0276 Initial Pb(II) Concentration * NTSAC dose - 0.0664

470 Initial Pb(II) Concentration * pH - 0.000884 Initial Pb(II) Concentration * Contact time + 0.4300

471   NTSAC dose * pH - 0.0287 WHAC dose * Contact time - 0.09667 pH * Contact time - 0.00278

472   Initial Pb(II) Concentratiion² - 3.539 NTSAC dose² - 9.524 pH² - 0.003014 Contact time²

473   (15)

474   **3.3 Statistical analysis**

475   To determine the effect of each process variable on NTSAC's adsorption efficacy towards Pb(II)

476   ions from the solution, an analysis of variance (ANOVA) was performed, and the findings are

477   shown in Table 5. When the p-values of the model terms were less than 0.05, the model terms were

significant (Kowalczyk et al., 2021). Thus, the stated factors and the impact of their interactions affect for the adsorption of Pb(II) ions onto NTSAC were significant, suggesting that the independent components were substantial. In this line, many previous studies on bio-adsorbents made from agricultural waste have reached the same conclusion. With a p-value higher than 0.0001 and an F-value of 82.65, the model showed that the Pb(II) ions adsorption process was well-fitted by the developed model (Eq. 15).

Table 5. ANOVA and coefficient of regression for the quadratic model for the adsorptive elimination of Pb(II) ions from aqueous medium using NTSAC

Source	Sum of Squares	df	Mean Square	F-value	p-value	
Model	1580.69	14	112.91	72.49	< 0.0001	significant
A-Initial Cr (VI) Concentration	52.01	1	52.01	33.39	< 0.0001	
B-NTSAC dose	9.70	1	9.70	6.23	0.0247	
C-pH	219.11	1	219.11	140.67	< 0.0001	
D-Contact time	15.31	1	15.31	9.83	0.0068	
AB	19.49	1	19.49	12.51	0.0030	
AC	28.20	1	28.20	18.10	0.0007	
AD	18.02	1	18.02	11.57	0.0039	
BC	0.7396	1	0.7396	0.4748	0.5013	
BD	11.87	1	11.87	7.62	0.0146	
CD	33.64	1	33.64	21.60	0.0003	

|						
A²	541.27	1	541.27	347.51	< 0.0001	
B²	343.44	1	343.44	220.50	< 0.0001	
C²	155.50	1	155.50	99.84	< 0.0001	
D²	201.78	1	201.78	129.55	< 0.0001	
Residual	23.36	15	1.56			
Lack of Fit	9.88	10	0.9883	0.3665	0.9170	not significant
Pure Error	13.48	5	2.70			
Cor Total	1604.05	29				

486

3.4 Analysis of the effect of parameter interaction on the adsorption process

The current investigation employed the RSM-CCD approach to assess the influence of selected process variables, namely, initial Pb(II) concentration, dose of NTSAC, solution pH, and adsorption time. During examination of interaction effect, the two process components were held constant at their midpoint. The ensuing analysis made with the use of 3D response surface techniques to show the effect of two variables on Pb(II) ion adsorption in an interactive fashion (Figure 8). The interaction between adsorbent quantity and Initial Pb(II) concentration was explored in regard to the adsorption of Pb(II) ions from synthetic aqueous medium. The concentration ranges tested were 60 to 170 ppm of Pb(II) and the loading of the adsorbent range was 0.2 to 1 g/100 mL. According to Figure 8(A). Adsorbent dosage of 0.483g/100 mL and starting concentration of 88.87 ppm resulted in a maximum efficacy of 93.41% in Pb(II) ion removal. In contrast, there was no shift in either the adsorption duration or the pH of the solution. Reducing the initial Pb(II) ion concentration and increasing the NTSAC dosage indicate that the

500 adsorption process has been expedited. Since the initial concentration of Pb(II) ions was lower, the

501 increased surface area and number of adsorption sites on the NTSAC account for this result.

502
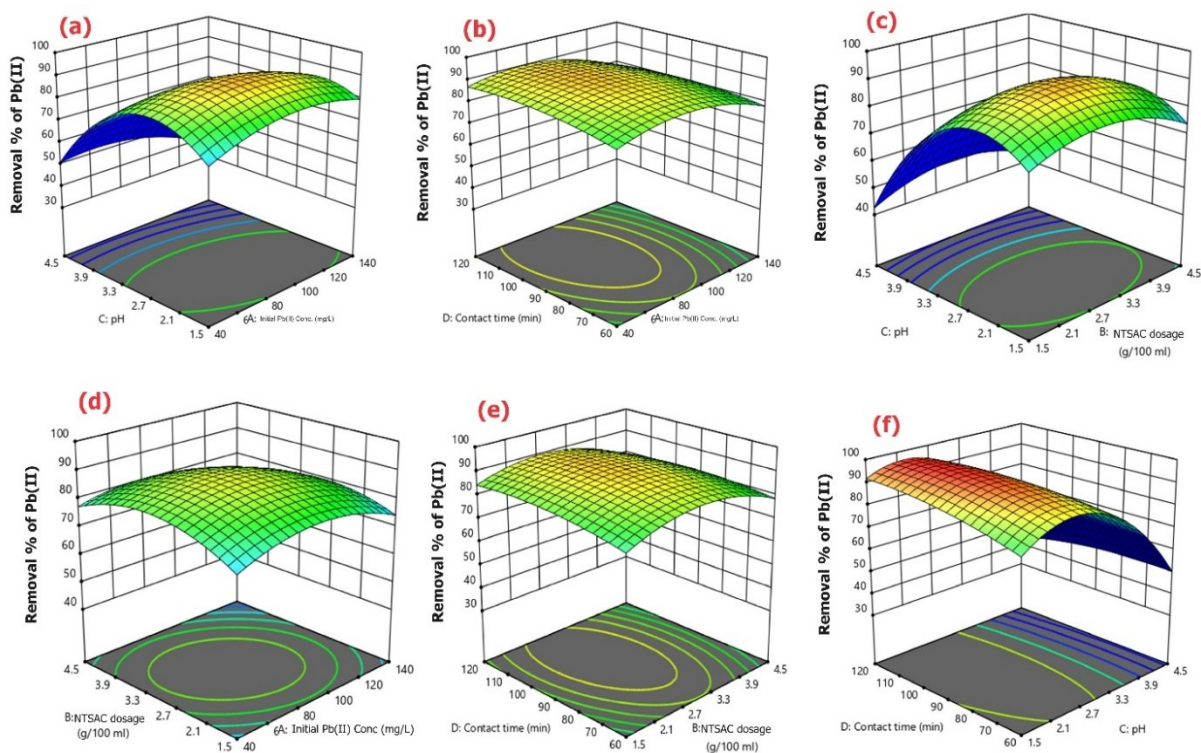
503

504 Figure 8. Illustration of interaction effect on the chosen parameters for Pb(II) adsorption.

505

506 This strengthens the connection between the molecule and the NTSAC because the ions are more

507 likely to stick to the empty adsorbent surface. The adsorption rate, however, slowed down with

508 increasing lead molecule concentrations due to site saturation and competition among Lead (II)

509 ions for the finite number of accessible necessary sites. As the initial concentrations of lead ions

510 in aqueous medium via adsorbent increased, the effectiveness of metal removal decreased,

511 according to Khanniri et al., in agreement with the findings of this investigation (Khanniri et al.,

512 2023). The effectiveness of removing Lead (II) ions was found to be greater than 80% when the

513 adsorbent dosage was increased from 0.2 to 0.8g/100 mL and the initial Pb(II) concentration was

514 raised from 40 to 80 ppm. When Pb(II) concentrations were too high, the active sites necessary for

515 ion adsorption was exhausted. This decreases the adsorbent's overall efficiency. In this vein, Bayuo

516 et al. reported on similar experiments (Bayuo et al., 2023).

517 On the following adsorption of Pb(II) ions by NTSAC, the statistical significance of the

518 relationship between initial Pb(II) ion concentration (40-160 ppm) and adsorption period (50-110

519 min) was evaluated ($p = 0.0001$). With a modest adsorbent dosage and solution pH, an initial Pb(II)

520 concentration ranging from 45 to 110 ppm, and an adsorbed duration of 40 to 90 min, NTSAC

521 attained an adsorption effectiveness of over 92%. With an initial ion concentration of 88.7 ppm,

522 an adsorb duration of 90 min, and intermediate values of NTSAC dosage and pH value, the

523 maximum Pb(II) absorption efficiency was 94.4%. At lower concentrations of Pb(II) ions, a larger

524 number of ions can be joined to the adsorbent's available surface area because of NTSAC's low

525 dissolved ion to site ratio. Adsorption efficiency decreases with increasing Pb(II) ions

526 concentration, likely because adsorbate compete for a finite number of active sites hence the

527 adsorption sites have become overloaded. Figure 8(b) shows that because there were more active

528 sites available during the first stage of contact, the adsorption rate was higher. The entire surface

529 area was filled up as time went on and more Pb(II) ions were adsorbed onto the adsorbent. Şeyda

530 et al. have examined on the groundnut shell-based adsorbent to capture Pb(II) ions from the

531 synthetic solution. According to their findings, the adsorbent maintained a steady removal

532 efficiency thereafter, with the peak removal efficiency of 90.26% recorded after 90 min (Taşar et

533 al., 2014).

534 The 3D surface plot of the interaction between the A and C of the solution is illustrated in Figure

535 8(c). The statistical significance of the interaction effect on Pb(II) removal was supported by a p-

536 value of 0.0425. The solution's pH is a major influence in the efficiency with which different

537 adsorbents that can remove heavy metals. Figure 8(c) illustrates that as the pH of the solution

538 increased from 2 to 5.5, the adsorption process of ions from the medium was boosted. At pH 5.5,

539 NTSAC exhibited its highest capacity for adsorbing Pb(II) ions from aqueous solutions. The

540 adsorption process was less successful at pH values below and above 5.5. Aside from adsorption

541 site competition and solution pH, the net charge of functional groups on the NTSAC surface also

542 influences the ionic state of Pb(II). Media hydrogen ion concentration and the adsorption

543 competition between Pb(II) ions and positive ligand surfaces at low pH were controlled by an

544 anionic binding site on NTSAC's active surface area. This led to reduced electrostatic interaction

545 between the NTSAC particles and Pb(II) ions. However, at high pH levels, the adsorption capacity

546 is reduced by adsorbed hydroxo ions $[Pb(OH)^+]$ and/or precipitates of $Pb(OH)_2$ present in the

547 medium. As a result, the NTSAC surfaces have less Pb(II) on them. In such a way, Awual et al.

548 observed comparable outcomes, specifying that the optimal solution pH range for removing Pb(II)

549 ions from a synthetic medium was between 2 and 8. Furthermore, they determined that the

550 adsorbent achieved its maximum efficacy in adsorbing Pb(II) ions at a pH of 5.2 (Ghasemi et al.,

551 2014).

552 Figure 8(d) shows the correlation between the lead (II) ion adsorption by NTSAC of the following

553 variables: base concentration, pH of the solution, dose of the adsorbent, and contact/adsorption

554 duration. Using a p-value of 0.0266, the effect of interaction was found to be statistically

555 significant. The results demonstrated that as the concentration of NTSAC increased from 0.2 to

556 0.8g/100mL and the adsorption time from 50 to 90 minutes, the adsorption process improved. The

557   interaction impact between adsorbent amount and solution pH during the removal of Pb(II) ions is

558   illustrated in Figure 8(e). The significance of their interaction effects was further established by a

559   p-value of 0.0432. According to Figure 8(f), a notable relationship between the adsorption period

560   and solution pH of the media (p-value = 0.0272) was also seen during the lead adsorption process

561   from aqueous media.

562   **3.5 Parametric optimization for maximized removal of Pb(II) ions**

563   In order to ascertain the relevance of the optimization result under the projected optimal points of

564   the CCD design model, triple tests were conducted. Table 6 presents the adsorption of Pb(II) ions

565   by NTSAC, with the best possible settings for the chosen variables. Removal effectiveness of

566   NTSAC at the ideal concentrations was measured experimentally, and the mean value was very

567   close to the value predicted by the model. This validation therefore demonstrates that the quadratic

568   model was well-appropriate for this procedure.

569   Table 6: Adsorption of Pb(II) ions by NTSAC, with the best possible settings for the chosen

570   variables

Processing factors	Initial Lead (II) concentration (ppm)	Adsorption time (min)	NTSAC dose (g/100mL)	Solution pH	Removal efficacy (%)		Desirability
					Predicted	Actual	
Optimized conditions	95.355	87.531	0.655	5.6	92.96	90.89	1

571   The present study's maximal adsorption capabilities were compared in relation to the results

572   obtained from previous research (Table 7). The adsorption of Pb(II) ions was accomplished

573 through the utilisation of adsorbents obtained from several sources of agricultural waste. In

574 comparison to other agricultural waste-based activated carbon, the ABC prepared teff-straw has

575 an adequate importance for Pb(II) ion adsorption (42.97 mg/g).

576 Table 7. Comparison of Pb(II) ion adsorption capabilities on different sorbents

Adsorbent	Q_{max} (mg/g)	References
Fig sawdust	80.64	(Ghasemi et al., 2014)
Sawdust of meranti	34.25	(Rafatullah et al., 2009)
Carbon obtained from Mentha piperita	53.19	(Ahmad & Haseeb, 2017)
Date pits activated carbon	30.70	(Brown et al., 2000)
Powder of peanut hull	30.43	(Abdulkarim & Al-Rub, 2004)
Waste Algal biomass	44.00	(Vilar et al., 2005)
NTSAC	43.97	Present study

577

578 **3.6 Adsorption isotherms**

579 Three isotherm models were used for the examination of the equilibrium data: Dubinin-

580 Radushkevich (D-R), Freundlich (F), and Temkin (T). The outcomes of utilizing equations (3)

581 through (11) to compute the adsorption parameters of the different models are presented in Table

582 8. The manner in which the models forecast the outcomes of the experiments is seen in Figure 9.

583 The D-R, F, L, and T isotherm models yielded the R^2 values of 0.985, 0.927, 0.939, and 0.953,

584 respectively, for the NTSAC adsorbent. This demonstrates that, relative to the other models

585   evaluated, the experimental results were most accurately characterized by the Langmuir (L)

586   isotherm. The nonlinear thermodynamic data, the maximum adsorption capacity, and the fitting

587   parameter (k_L) of the Langmuir model are presented in Table 8 and Figure 9, respectively.

588   According to the L model, the adsorption of sodium ions onto the surface of biomass occurs in a

589   homogeneous and monolayer fashion, suggesting that no interaction has taken place among the

590   Pb(II) ions. Furthermore, separation factor (R_L) which is an additional characteristic of the

591   Langmuir equilibrium model. Theoretically, the isotherm is unfavorable if R_L is greater than one,

592   linear if R_L equals one, reversible if R_L equals zero, and favorable if R_L is less than one. The

593   calculation of the R_L is possible via the subsequent equation (16).

$$R_L = \frac{1}{1+k_L*C_i} \hspace{4cm} (16)$$

594   where, C_i initial Pb (II) concentration, k_L is Langmuir constant, and $R_L = 0.144$.

595   Because the value of R_L was observed to be between 0 and 1, it is determined that the adsorption

596   of Pb(II) ions was sufficient. Furthermore, it was determined that the highest viable capacity for

597   monolayer adsorption (q_m) was 71.17 mg/g. However, the maximal monolayer adsorption capacity

598   (q_m) of the present bio-adsorbent was marginally greater.

599   Table 8. Linear fit of the isotherm model constants for Pb(II) on NTSAC.

Isotherm model	Factors determined from the linear model fit
Langmuir	$k_L = 0.0010943$ L/mg; $q_m = 73.08$ (mg/g); $R^2 = 0.985$
Freundlich	$k_F = 4.052$ (mg/g)(L/mg)$^{1/n}$; $1/n = 0.543$; $R^2 = 0.927$
Temkin	$k_T = 0.01358$; $b_T = 165.74$; $R^2 = 0.936$
D-R	$q_m = 59.8292$; $E = 2.914$; $k_D = 0.0590$; $R^2 = 0.964$

600   As shown in Table 8 displays the nonlinear thermodynamic data (k_F), while Figure 7(b) displays

601   the fitting parameters (n) for the Freundlich model. Intermolecular adsorption and surface

602   adsorption affinity variation are both modelled by the Freundlich equation for ions adsorbed on

603   heterogeneous surfaces. A pre-established value of n, which denotes the degree of isothermal

604   favorability, and the Freundlich constant (K_F) can be used to compute the adsorption capacity. The

605   equilibrium adsorption of sodium ions onto the bio-sorbent can be described by its adsorption

606   coefficient, k_F. When measuring affinity to a sorbent, a greater k_F value indicates a stronger bond.

607   The heterogeneity of the adsorbent's surface is represented by the Freundlich model parameter n.

608   Leaner absorption occurs when n = 1, while chemical adsorption happens when n > 1, and physical

609   adsorption happens when n < 1. The current bio-adsorbent had a n value of 3.09, suggesting Pb(II)

610   ions were physically adsorbing onto the biomass. However, when compared to the Langmuir

611   model's values, the Freundlich model's R^2 was inadequate. Figure 9 illustrates the non-linear fitting

612   of the experimental isotherm data to the Temkin isotherm model. R^2 values indicated that the T

613   isotherm model did not appear to well describe the adsorption data. Conversely, the D-R model

614   exhibits a stronger correspondence with the data in relation to the Langmuir isotherm model and

615   was less favorably correlated with the Freundlich and Temkin isotherm models.

616

617
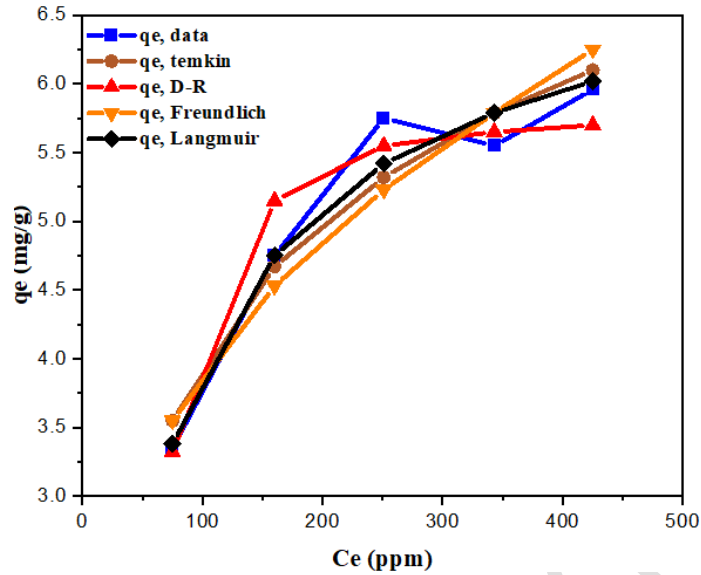
Figure 9. The equilibrium uptake adsorption isotherms for Pb(II) adsorption.

3.7 Adsorption kinetics

The experimental adsorption data was subjected to examine the following kinetic models: pseudo-first-order, second-order, intra-particle diffusion, and Elovich in order to ascertain the rate of Pb(II) adsorption and comprehend the process. Aforementioned models have been employed to fit the experimental findings. The fitting processes' findings are presented in Table 9. The observed constants from the fittings of kinetics model were used to depict the adsorption data and the values anticipated by the models stated before (Figure 10).

Nevertheless, the R^2 value observed by the pseudo-2nd-order model was 0.999. Experimental data and pseudo-second-order model predictions for q_e for bio-adsorbent were very congruent. This showed that the kinetics data obtained from experimentation for the current biosorbent were best fit by the pseudo-second-order model. A lot of studies have looked at the removal of Pb(II) ions from aqueous media using various adsorbents, and they all exhibited to the same conclusion.

631

632
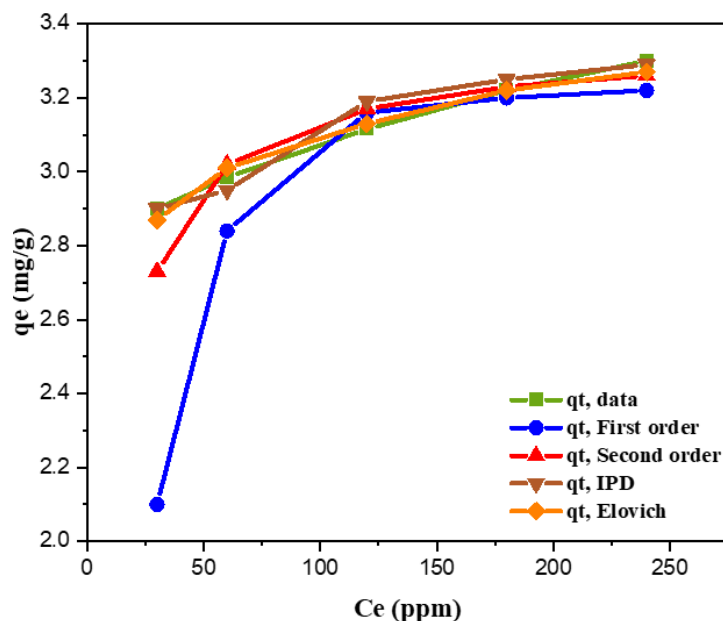
633   Adsorption of Pb(II)ions into the bio-adsorbent was shown to be rate-limiting, and this was

634   determined by testing the intraparticle diffusion model. Depends on intraparticle diffusion kinetic

635   model, R^2 value was calculated to be 0.983; showing the significance of intraparticle diffusion in

636   adsorption. It was apparent that the intraparticle diffusion kinetic model may account for the

637   apparent experimental findings. Comparable in value to the values documented for the adsorptive

638   uptake of additional metal ions from liquids, the intraparticle diffusion rate constant (k_{dif}) was

639   determined to be 0.415 mg/g mim$^{0.5}$. The values of boundary layer thickness (C), which serve as

640   indicators of resistance to external mass transfer, was recorded as 23.971 mg/g. The C values of

641   the present bio-adsorbent for heavy metal removal were similar to those of other bio-adsorbents

642   reported in the scientific literature.

643   In order to evaluate chemisorption nature of the adsorption process, Elovich kinetic model has

644   been investigated using the adsorption data. In this regard, the R^2 value for the Elovich model's fit

645   to the kinetic data was 0.976. The experimental findings were most well elucidated by the Elovich

646   model, which emphasized the benefits of chemisorption occurring on a heterogeneous surface.

647   Diffusion from the bulk to the surface and chemisorption, in which electrons are shared or

648   exchanged between the adsorbent and the adsorbate, both have a role in regulating the rate at which

649   Pb ions interact with the bio-adsorbent. For the cation interaction with lignocellulose materials,

650   similar fits to isotherms and kinetics were reported from prior investigations.

651   Table 9. Linear fit kinetic model constants for Pb(II) adsorption on NTSAC.

Kinetic Model	Factors		Kinetic models fitting factors
Pseudo-first order	q_e (mg/g)	Experimental	32.964
		Model	32.154
	k_1 (min^{-1})		0.0353
	R^2		0.784
Pseudo-second order	q_e (mg/g)	Experimental	36.784
		Model	36.599
	k_2 (g/ mg. min.)		0.145
	R^2		0.999
Intra-particle diffusion	k_{dif} (mg/g.mim$^{0.5}$)		0.405
	C (mg/g)		26.708
	R^2		0.983
Elovic	a_E (mg/(g min))		0.517

	b_E (mg/(g min))	164299.1
	R^2	0.966

652

3.8 Characteristic examination of adsorbent using XPS analysis

654 XPS tests were conducted on biochar subsequent to sorption in order to delve deeper into the

655 adsorption mechanism. The acquired biocarbon was characterized using X-ray photoelectron

656 spectroscopy (XPS) prior to and subsequent to Pb^{2+} adsorption in order to analyze alterations in

657 the chemical environment and binding energy of the ions under investigation. For C1s, Pb4f, and

658 O1, the survey curves are illustrated in Figure 11. According to the results, the maximum binding

659 energies of C-C groups, C-O groups, and O = C-O groups were approximately 285.7 eV, 286.8

660 eV, and 289.8 eV, respectively. The following peaks were identified: C-O, O-H, and C = O-O at

661 532.37 eV, 533 eV, and 533.52 eV, respectively; Pb(II) and Pb-O at 140 eV and 142.8 eV,

662 respectively. Following Pb(II) adsorption, the binding energies of these peaks underwent a

663 negligible alteration. As illustrated in Figure 11(a), the adsorbent experiences a reduction in its C-

664 O to C-O ratio due to the adsorption of Pb(II). The morphological changes that occur throughout

665 the adsorption process were shown by the abundance of hydroxyl and carboxyl groups. With the

666 addition of Pb(II), the adsorbed sample's peak areas of O-H and Pb-O increased significantly. A

667 large amount of Pb-O-H was produced during the adsorption process, as shown by the observed

668 changes. Peaks for Pb(II) and Pb-O in the post-adsorption phase show that physical and chemical

669 adsorption occurred during the process.
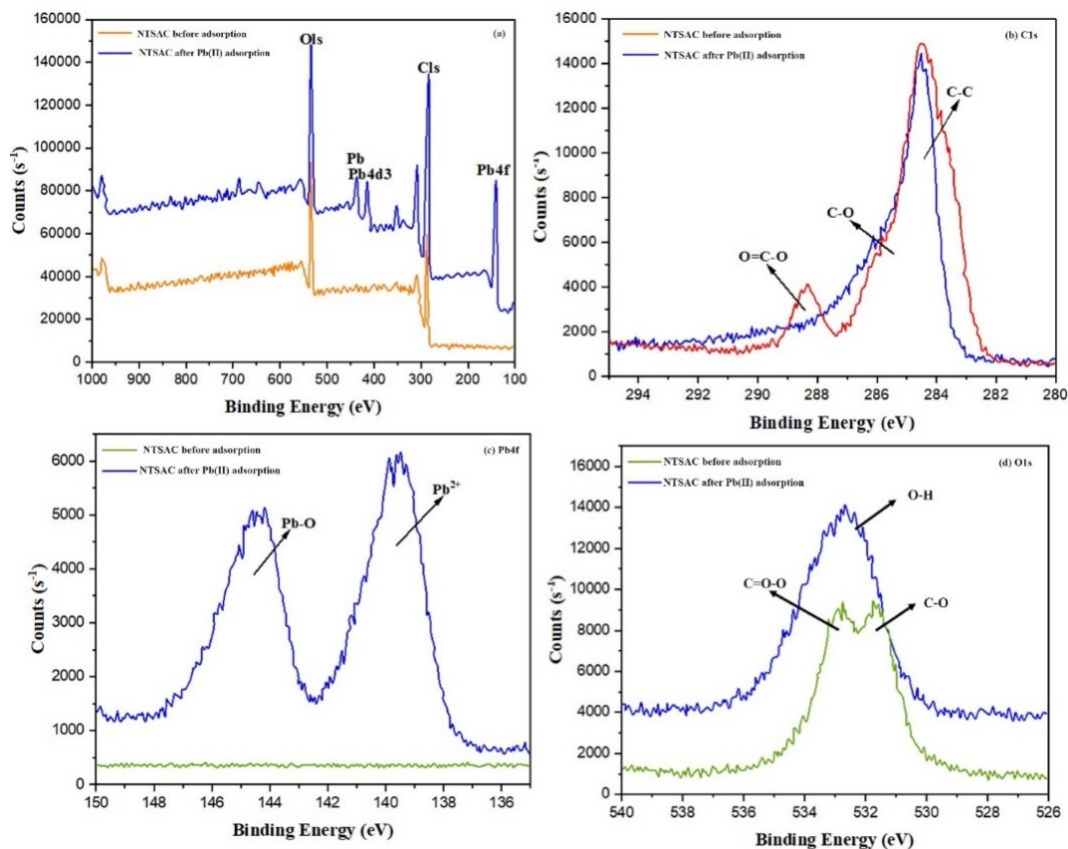
Figure 11. The XPS profiles of biochar before and after adsorption Pb(II)

4. Conclusion

Straw obtained from teff (Eragrostis tef), an annual grass, as a specialty crop of Ethiopia was examined for its ability to adsorb Pb(II) ions. Nano-scaled magnetized activated carbon (NTSAC) was derived from teff straw and the properties of the NTSAC were ascertained through the use of FTIR, XRD, SEM, BET, and PZC studies. Selective independent factors, such as the initial Pb(II) concentration of, the dose of NTSAC, the solution pH, and the contact time, were optimized using batch adsorption studies employing response surface methods (RSM) in conjunction with CCD matrix. The optimal value from the statistical optimization were as follows: 95.36 mg/L, 0.656

681   g/100 mL, 5.5, and 88.7 min, respectively. According to isotherms studies, the most precise

682   outcomes were obtained to be well-fitted to the Langmuir isotherm. The kinetic study revealed

683   that the NTASC's Pb(II) ion adsorption rate was found to be suited with the pseudo-second-order

684   model. From the findings, NTSAC exhibits promise as a low-cost bioadsorbent for the removal of

685   harmful Pb(II) ions from contaminated water because it is inexpensively manufactured from

686   locally accessible Ethiopian agricultural waste.

687

Declarations:

689   **Ethical approval**: Not applicable.

690   **Competing interest**: Not applicable.

691   **Conflict of interest**: The authors declare that they have no conflict of interests.

692   **Consent for publication**: All authors agree to the publishing of the paper.

693   **Acknowledgement:**

696

697   **Availability of data and materials**: Will be provided based on request to corresponding author

698   **Author contributions**

699   **M S**. Designed experiments, supervised, **SB**. Wrote initial draft and edited the manuscript, **VS**.

700   carried out investigation, **VPS**. Validation, characterization and edited the manuscript, **SM**. wrote

701   initial draft and edited the manuscript, **SK**. Funding acquisition, and **JMK:** characterization and

702   software analysis.

703

Reference

Abdulkarim, M., & Al-Rub, F. A. (2004). Adsorption of lead ions from aqueous solution onto activated carbon and chemically-modified activated carbon prepared from date pits. *Adsorption Science and Technology*, *22*(2), 119–134. https://doi.org/10.1260/026361704323150908

Ahmad, R., & Haseeb, S. (2017). Adsorption of Pb(II) on Mentha piperita carbon (MTC) in single and quaternary systems. *Arabian Journal of Chemistry*, *10*, S412–S421. https://doi.org/10.1016/j.arabjc.2012.09.013

Aiyesanmi, A. F., Adebayo, M. A., & Fadairo, F. F. (2022). Evaluation of avocado pear seed coat for removal of nickel and chromium ions from aqueous solution. *Journal of Hazardous, Toxic, and Radioactive Waste*, *26*(4), 04022027.

Al-Hazmi, G. A. A., El-Zahhar, A. A., El-Desouky, M. G., & El-Bindary, A. (2024). Superior adsorption and removal of doxorubicin from aqueous solution using activated carbon via thermally treated green adsorbent: isothermal, kinetic, and thermodynamic studies. *Environmental Technology (United Kingdom)*, *45*(10), 1969–1988. https://doi.org/10.1080/09593330.2022.2159540

Ameen, M., Zamri, N. M., May, S. T., Azizan, M. T., Aqsha, A., Sabzoi, N., & Sher, F. (2022). Effect of acid catalysts on hydrothermal carbonization of Malaysian oil palm residues (leaves, fronds, and shells) for hydrochar production. *Biomass Conversion and Biorefinery*, *12*, 103–114.

724 Awad, A. M., Jalab, R., Benamor, A., Nasser, M. S., Ba-Abbad, M. M., El-Naas, M., &

725 Mohammad, A. W. (2020). Adsorption of organic pollutants by nanomaterial-based

726 adsorbents: An overview. *Journal of Molecular Liquids*, *301*, 112335.

727 Aziz, M. A., Zubair, M., Saleem, M., Alharthi, Y. M., Ashraf, N., Alotaibi, K. S., Aga, O., & Al

728 Eid, A. A. A. (2023). Mechanical, non-destructive, and thermal characterization of biochar-

729 based mortar composite. *Biomass Conversion and Biorefinery*.

730 https://doi.org/10.1007/s13399-023-03838-1

731 Bagali, S. S., Gowrishankar, B. S., & Roy, A. S. (2017). Optimization, kinetics, and equilibrium

732 studies on the removal of lead (II) from an aqueous solution using banana pseudostem as an

733 adsorbent. *Engineering*, *3*(3), 409–415.

734 Balasubramanian, B., Meyyazhagan, A., Chinnappan, A. J., Alagamuthu, K. K., Shanmugam, S.,

735 Al-Dhabi, N. A., Ghilan, A. K. M., Duraipandiyan, V., & Arasu, M. V. (2020). Occupational

736 health hazards on workers exposure to lead (Pb): A genotoxicity analysis. *Journal of Infection*

737 *and Public Health*, *13*(4), 527–531.

738 Bayuo, J., Rwiza, M. J., & Mtei, K. M. (2023). Non-competitive and competitive detoxification of

739 As(III) ions from single and binary biosorption systems and biosorbent regeneration. *Biomass*

740 *Conversion and Biorefinery*. https://doi.org/10.1007/s13399-022-03734-0

741 Beyan, S. M., Ambio, T. A., Sundramurthy, V. P., Gomadurai, C., & Getahun, A. A. (2024).

742 Adsorption phenomenon for removal of Pb (II) via teff straw based activated carbon prepared

743 by microwave-assisted pyrolysis: process modelling, statistical optimisation, isotherm,

744 kinetics, and thermodynamic studies. *International Journal of Environmental Analytical*

745 *Chemistry*, *104*(4), 916–937.

746 Brown, P., Atly Jefcoat, I., Parrish, D., Gill, S., & Graham, E. (2000). Evaluation of the adsorptive

747   capacity of peanut hull pellets for heavy metals in solution. *Advances in Environmental*

748   *Research*, *4*(1), 19–29. https://doi.org/10.1016/S1093-0191(00)00004-6

749 Cao, S., Cao, J., Zhu, H., Huang, Y., Jin, B., & Materazzi, M. (2024). Removal of HCl from gases

750   using modified calcined Mg-Al-CO3 hydrotalcite: Performance, mechanism, and adsorption

751   kinetics. *Fuel*, *355*, 129445.

752 Chen, Y., Wang, H., Ying, Z., & Gao, Q. (2020). Ibudilast enhances the clearance of SOD1 and

753   TDP-43 aggregates through TFEB-mediated autophagy and lysosomal biogenesis: The new

754   molecular mechanism of ibudilast and its implication for neuroprotective therapy.

755   *Biochemical and Biophysical Research Communications*, *526*(1), 231–238.

756 Dąbrowski, A. (2001). Adsorption—from theory to practice. *Advances in Colloid and Interface*

757   *Science*, *93*(1–3), 135–224.

758 Danish, M., Ansari, K. B., Danish, M., Khatoon, A., Rao, R. A. K., Zaidi, S., & Aftab, R. A.

759   (2022). A comprehensive investigation of external mass transfer and intraparticle diffusion

760   for batch and continuous adsorption of heavy metals using pore volume and surface diffusion

761   model. *Separation and Purification Technology*, *292*, 120996.

762 Debnath, S., & Das, R. (2023). Strong adsorption of CV dye by Ni ferrite nanoparticles for waste

763   water purification: Fits well the pseudo second order kinetic and Freundlich isotherm model.

764   *Ceramics International*, *49*(10), 16199–16215.

765 Dong, J., Shen, L., Shan, S., Liu, W., Qi, Z., Liu, C., & Gao, X. (2022). Optimizing magnetic

766   functionalization conditions for efficient preparation of magnetic biochar and adsorption of

Pb(II) from aqueous solution. *Science of the Total Environment*, *806*. https://doi.org/10.1016/j.scitotenv.2021.151442

Duan, R., Chen, Y., Zhou, Y., Long, L., Jiang, Z., & Chen, X. (2023). Adsorption Optimization of Methylene Blue from Aqueous Solution by Cost-Effective Biochar Using Response Surface Methodology and a Modeling Approach. *Water, Air, & Soil Pollution*, *234*(11), 690.

Foroutan, R., Mohammadi, R., Adeleye, A. S., Farjadfard, S., Esvandi, Z., Arfaeinia, H., Sorial, G. A., Ramavandi, B., & Sahebi, S. (2019). Efficient arsenic(V) removal from contaminated water using natural clay and clay composite adsorbents. *Environmental Science and Pollution Research*, *26*(29), 29748–29762. https://doi.org/10.1007/s11356-019-06070-5

Gan, I., & Chow, W. S. (2021). Tailoring Chemical, Physical, and Morphological Properties of Sugarcane Bagasse Cellulose Nanocrystals via Phosphorylation Method. *Journal of Natural Fibers*, *18*(10), 1448–1459. https://doi.org/10.1080/15440478.2019.1691120

Ghasemi, M., Naushad, M., Ghasemi, N., & Khosravi-fard, Y. (2014). A novel agricultural waste based adsorbent for the removal of Pb(II) from aqueous solution: Kinetics, equilibrium and thermodynamic studies. *Journal of Industrial and Engineering Chemistry*, *20*(2), 454–461. https://doi.org/10.1016/j.jiec.2013.05.002

Gonçalves, M., Guerreiro, M. C., Oliveira, L. C. A., Solar, C., Nazarro, M., & Sapag, K. (2013a). Micro mesoporous activated carbon from coffee husk as biomass waste for environmental applications. *Waste and Biomass Valorization*, *4*(2), 395–400. https://doi.org/10.1007/s12649-012-9163-1

787   Gonçalves, M., Guerreiro, M. C., Oliveira, L. C. A., Solar, C., Nazarro, M., & Sapag, K. (2013b).

788   Micro mesoporous activated carbon from coffee husk as biomass waste for environmental

789   applications. *Waste and Biomass Valorization*, *4*, 395–400.

790   Guel-Nájar, N. A., Rios-Hurtado, J. C., Muzquiz-Ramos, E. M., Dávila-Pulido, G. I., González-

791   Ibarra, A. A., & Pat-Espadas, A. M. (2023). Magnetic Biochar Obtained by Chemical

792   Coprecipitation and Pyrolysis of Corn Cob Residues: Characterization and Methylene Blue

793   Adsorption. *Materials*, *16*(8). https://doi.org/10.3390/ma16083127

794   Hu, J., & Shipley, H. J. (2012). Evaluation of desorption of Pb (II), Cu (II) and Zn (II) from

795   titanium dioxide nanoparticles. *Science of the Total Environment*, *431*, 209–220.

796   Huang, J., Cao, Y., Liu, Z., Deng, Z., Tang, F., & Wang, W. (2012). Efficient removal of heavy

797   metal ions from water system by titanate nanoflowers. *Chemical Engineering Journal*, *180*,

798   75–80.

799   Igalavithana, A. D., Mandal, S., Niazi, N. K., Vithanage, M., Parikh, S. J., Mukome, F. N. D.,

800   Rizwan, M., Oleszczuk, P., Al-Wabel, M., & Bolan, N. (2017). Advances and future

801   directions of biochar characterization methods and applications. *Critical Reviews in*

802   *Environmental Science and Technology*, *47*(23), 2275–2330.

803   Ighalo, J. O., & Adeniyi, A. G. (2020). Adsorption of pollutants by plant bark derived adsorbents:

804   an empirical review. *Journal of Water Process Engineering*, *35*, 101228.

805   Jagadeesh, N., & Sundaram, B. (2023). Adsorption of pollutants from wastewater by biochar: a

806   review. *Journal of Hazardous Materials Advances*, *9*, 100226.

807 Karuppaiyan, J., Jeyalakshmi, R., Kiruthika, S., Wadaan, M. A., Khan, M. F., & Kim, W. (2023).

808 A study on the role of surface functional groups of metakaolin in the removal of methylene

809 blue: Characterization, kinetics, modeling and RSM optimization. *Environmental Research*,

810 *226*, 115604.

811 Khanniri, E., Yousefi, M., Mortazavian, A. M., Khorshidian, N., Sohrabvandi, S., Koushki, M. R.,

812 & Esmaeili, S. (2023). Biosorption of cadmium from aqueous solution by combination of

813 microorganisms and chitosan: response surface methodology for optimization of removal

814 conditions. *Journal of Environmental Science and Health - Part A Toxic/Hazardous*

815 *Substances and Environmental Engineering*, *58*(5), 433–446.

816 https://doi.org/10.1080/10934529.2023.2188023

817 Kifetew, M., Alemayehu, E., Fito, J., Worku, Z., Prabhu, S. V., & Lennartz, B. (2023). Adsorptive

818 removal of reactive yellow 145 dye from textile industry effluent using Teff Straw Activated

819 Carbon: Optimization using central composite design. *Water*, *15*(7), 1281.

820 Kowalczyk, P., Ligas, B., Skrzypczak, D., Mikula, K., Izydorczyk, G., Witek-Krowiak, A.,

821 Moustakas, K., & Chojnacka, K. (2021). Biosorption as a method of biowaste valorization to

822 feed additives: RSM optimization. *Environmental Pollution*, *268*.

823 https://doi.org/10.1016/j.envpol.2020.115937

824 Kumar, V., Dwivedi, S. K., & Oh, S. (2022). A critical review on lead removal from industrial

825 wastewater: Recent advances and future outlook. *Journal of Water Process Engineering*, *45*,

826 102518.

827 Leite, A. B., Saucier, C., Lima, E. C., Dos Reis, G. S., Umpierres, C. S., Mello, B. L., Shirmardi,

828 M., Dias, S. L. P., & Sampaio, C. H. (2018). Activated carbons from avocado seed:

829   optimisation and application for removal of several emerging organic compounds.

830   *Environmental Science and Pollution Research*, *25*, 7647–7661.

831   Levin, R., Vieira, C. L. Z., Rosenbaum, M. H., Bischoff, K., Mordarski, D. C., & Brown, M. J.

832   (2021). The urban lead (Pb) burden in humans, animals and the natural environment.

833   *Environmental Research*, *193*, 110377.

834   Merine, M. K., Venkatesa Prabhu, S., Worku, Z., Fito, J., & Alemayehu, E. (2024). Adsorptive

835   removal of reactive yellow 145 dye from textile industry effluents using teff straw-activated

836   carbon: RSM-based process optimization. *Water Practice & Technology*, *19*(2), 362–383.

837   Mohammadpour, A., Karami, N., Zabihi, R., Fazeliyan, E., Abbasi, A., Karimi, S., de Farias, M.

838   B., Vieira, M. G. A., Shahsavani, E., & Khaneghah, A. M. (2023). Green synthesis,

839   characterization, and application of Fe3O4 nanoparticles for methylene blue removal: RSM

840   optimization, kinetic, isothermal studies, and molecular simulation. *Environmental Research*,

841   *225*, 115507.

842   Mohan, D., Kumar, H., Sarswat, A., Alexandre-Franco, M., & Pittman, C. U. (2014). Cadmium

843   and lead remediation using magnetic oak wood and oak bark fast pyrolysis bio-chars.

844   *Chemical Engineering Journal*, *236*, 513–528. https://doi.org/10.1016/j.cej.2013.09.057

845   Naidu, R., Biswas, B., Willett, I. R., Cribb, J., Singh, B. K., Nathanail, C. P., Coulon, F., Semple,

846   K. T., Jones, K. C., & Barclay, A. (2021). Chemical pollution: A growing peril and potential

847   catastrophic risk to humanity. *Environment International*, *156*, 106616.

848   Oliveira, L. C. A., Pereira, E., Guimaraes, I. R., Vallone, A., Pereira, M., Mesquita, J. P., & Sapag,

849   K. (2009). Preparation of activated carbons from coffee husks utilizing FeCl3 and ZnCl2 as

850   activating agents. *Journal of Hazardous Materials*, *165*(1–3), 87–94.

851   Qasem, N. A. A., Mohammed, R. H., & Lawal, D. U. (2021). Removal of heavy metal ions from

852   wastewater: A comprehensive and critical review. *Npj Clean Water*, *4*(1), 1–15.

853   Rafatullah, M., Sulaiman, O., Hashim, R., & Ahmad, A. (2009). Adsorption of copper (II),

854   chromium (III), nickel (II) and lead (II) ions from aqueous solutions by meranti sawdust.

855   *Journal of Hazardous Materials*, *170*(2–3), 969–977.

856   https://doi.org/10.1016/j.jhazmat.2009.05.066

857   Rahman, M. M., Alam, K., & Velayutham, E. (2021). Is industrial pollution detrimental to public

858   health? Evidence from the world's most industrialised countries. *BMC Public Health*, *21*(1),

859   1175.

860   Raj, K., & Das, A. P. (2023). Lead pollution: Impact on environment and human health and

861   approach for a sustainable solution. *Environmental Chemistry and Ecotoxicology*, *5*, 79–85.

862   Rose, P. K., Kumar, R., Kumar, R., Kumar, M., & Sharma, P. (2023). Congo red dye adsorption

863   onto cationic amino-modified walnut shell: Characterization, RSM optimization, isotherms,

864   kinetics, and mechanism studies. *Groundwater for Sustainable Development*, *21*, 100931.

865   Santhosh, C., Daneshvar, E., Tripathi, K. M., Baltrėnas, P., Kim, T. Y., Baltrėnaitė, E., &

866   Bhatnagar, A. (2020). Synthesis and characterization of magnetic biochar adsorbents for the

867   removal of Cr(VI) and Acid orange 7 dye from aqueous solution. *Environmental Science and*

868   *Pollution Research*, *27*(26), 32874–32887. https://doi.org/10.1007/s11356-020-09275-1

869   Sharmiladevi, S., Ramesh, N., Prabhu, S. V., & Mayakannan, S. (2024). Microwave-assisted

870   functionalized biosorbent preparation using seed gum of Tamarindus indica: characterization

871   and evaluation of Cr (VI) removal potency from tannery effluents. *Biomass Conversion and*

872   *Biorefinery*, 1–13.

873 Song, M., Jin, B., Xiao, R., Yang, L., Wu, Y., Zhong, Z., & Huang, Y. (2013). The comparison of

874   two activation techniques to prepare activated carbon from corn cob. *Biomass and Bioenergy*,

875   *48*, 250–256. https://doi.org/10.1016/j.biombioe.2012.11.007

876 Sundramurthy, V. P., Varadharajan, V., Wilson, V. H., Jose, S., Manoharan, S., Alharbi, N. S.,

877   Khaled, J. M., Kandasamy, B., & Palanisamy, G. (2024). Adsorptive removal of Cu (II) ions

878   from aqueous solution using Teff (Eragrostis tef) hay based magnetized biocarbon: RSM-

879   GA, ANN based optimization and kinetics aspects. *Zeitschrift Für Physikalische Chemie*, *0*.

880 Taşar, Ş., Kaya, F., & Özer, A. (2014). Biosorption of lead(II) ions from aqueous solution by

881   peanut shells: Equilibrium, thermodynamic and kinetic studies. *Journal of Environmental*

882   *Chemical Engineering*, *2*(2), 1018–1026. https://doi.org/10.1016/j.jece.2014.03.015

883 Tee, G. T., Gok, X. Y., & Yong, W. F. (2022). Adsorption of pollutants in wastewater via

884   biosorbents, nanoparticles and magnetic biosorbents: A review. *Environmental Research*,

885   *212*, 113248.

886 Tessema, B., Gonfa, G., Hailegiorgis, S. M., & Prabhu, S. V. (2023). Characteristic investigations

887   on bio-silica gel prepared from teff (eragrostis tef) straw: effect of calcination time. *Materials*

888   *Research Express*, *10*(11), 115102.

889 Varadharajan, V., Senthilkumar, D. S., Senthilkumar, K., Sundramurthy, V. P., Manikandan, R.,

890   Senthilarasan, H., Ganesan, H., Kesavamoorthy, I., & Ramasamy, A. (2022). Process

891   modeling and toxicological evaluation of adsorption of tetracycline onto the magnetized

892   cotton dust biochar. *Journal of Water Process Engineering*, *49*, 103046.

893 Vilar, V. J. P., Botelho, C. M. S., & Boaventura, R. A. R. (2005). Influence of pH, ionic strength
894 and temperature on lead biosorption by Gelidium and agar extraction algal waste. *Process*
895 *Biochemistry*, *40*(10), 3267–3275. https://doi.org/10.1016/j.procbio.2005.03.023

896 Wang, J., & Zhang, M. (2020). Adsorption characteristics and mechanism of bisphenol a by
897 magnetic biochar. *International Journal of Environmental Research and Public Health*,
898 *17*(3). DOI: 10.3390/ijerph17031075

899 Zhang, R., Qiao, Q., Liu, T., Zhao, J., Shi, S., Yuan, Y., & Wang, N. (2024). New insights into
900 hydration shells in boosting marine uranium adsorption kinetics. *Chemical Engineering*
901 *Journal*, *491*, 151995.

902 Zhao, H., Zhong, H., Jiang, Y., Li, H., Tang, P., Li, D., & Feng, Y. (2022). Porous ZnCl2-activated
903 carbon from shaddock peel: methylene blue adsorption behavior. *Materials*, *15*(3), 895.

904